IPEM
Institute of Physics and
Engineering in Medicine

ACCEPTED MANUSCRIPT • OPEN ACCESS

Characterization of susceptibility artifacts in magnetic resonance thermometry images during laser interstitial thermal therapy: dimension analysis and temperature error estimation

Characterization of Susceptibility artifacts in Magnetic Resonance Thermometry images during laser interstitial thermal therapy: dimension analysis and temperature error estimation.

Martina De Landro[a*], Cèline Giraudeau[b], Juan Verde[b], Khalid Ambarki[c], Sanzhar Korganbayev[a], Alexey Wolf[d], Henrik Odeen[e], Paola Saccomandi[a*]

[a] Department of Mechanical Engineering, Politecnico di Milano, Milan, Italy
[b] Institute of Image-Guided Surgery, Strasbourg, France
[c] Siemens Healthcare SAS Saint-Danis, France
[d] Laboratory of Fiber Optics, Institute of Automation and Electrometry of the SB RAS, 1 Academician Koptyug Ave., Novosibirsk, Russia.
[e] Department of Radiology and Imaging Science, University of Utah, Salt Lake City, UT, USA

*corresponding authors: martina.delandro@polimi.it; paola.saccomandi@polimi.it

Abstract

Objective. Laser interstitial thermal therapy (LITT) is a minimally invasive procedure used to treat a lesion through light irradiation and consequent temperature increase. Magnetic Resonance Thermometry Imaging (MRTI) provides a multidimensional measurement of the temperature inside the target thus enabling accurate monitoring of the zone of damage during the procedure. In proton resonance frequency shift-based thermometry, artifacts in the images may strongly interfere with the estimated temperature maps. In our work, after noticing the formation of the dipolar-behavior artifact linkable to magnetic susceptibility changes during *in vivo* LITT, an investigation of susceptibility artifacts in tissue-mimicking phantoms was implemented. *Approach.* The artifact was characterized: (i) by measuring the area and total volume of error regions and their evolution during the treatment; and (ii) by comparison with temperature reference provided by three temperature sensing needles. Lastly, a strategy to avoid artifacts formation was devised by using the temperature-sensing needles to implement a temperature-controlled LITT. *Main results.* The artifact appearance was associated with gas bubble formation and with unwanted treatment effects producing magnetic susceptibility changes when 2 W laser power was set. The analysis of the artifact's dimension demonstrated that in the sagittal plane the dipolar-shape artifact may consistently spread following the temperature trend until reaching a volume 8 times bigger than the ablated one. Also, the artifact shape is quite symmetric with respect to the laser tip. An absolute temperature error showing a negative Gaussian profile in the area of susceptibility artifact with values up to 64.4 °C was estimated. Conversely, a maximum error of 2.8 °C is measured in the area not-affected by artifacts and far from the applicator tip. Finally, by regulating laser power, susceptibility artifacts formation was avoided, and appreciable thermal damage was induced. *Significance.* Such findings may help in improving the MRTI-based guidance of thermal therapies.

Keywords
Laser interstitial thermal therapy, magnetic resonance thermometry imaging, susceptibility artifacts, temperature monitoring, fiber optic sensors.

1

1 Introduction

Laser interstitial thermal therapy (LITT) is a minimally invasive surgical procedure used to selectively treat a lesion using laser light (Odéen and Dennis L. Parker, 2019a). During LITT, a small flexible optical fiber delivering the therapeutic light is inserted in the target tissue, and the main effect produced from the tissue-light interaction is thermal one. Light absorbed by the tissue is converted into heat, thus inducing the coagulative necrosis of cells (Stafford *et al.*, 2010). Despite the LITT potential in the treatment of deep seated lesions and its efficacy for the treatment of tumors in several organs, including the brain (Salem *et al.*, 2019), the prostate (Walser *et al.*, 2019), the liver (Di Costanzo, Francica and Pacella, 2014), and the pancreas (Di Matteo *et al.*, 2018), widespread adoption in the clinical field has been slowed by still unsolved challenges relating to accurate and precise monitoring of the laser-induced thermal effects during the treatment (Patel, Patel and Danish, 2018).

The main goal of LITT is to induce coagulative necrosis in a well-circumscribed focal lesion of predictable dimensions. The effects of the thermal treatment on the tissue depend upon many factors, including temperature, applied energy, and tissue thermophysical properties (Bianchi *et al.*, 2022). Temperatures from 42 °C to 45 °C cause the inactivation of vital enzymes with consequent irreversible damage if they are applied for 30 to 60 minutes(Chu and Dupuy, 2014). The time required to achieve cell death decreases exponentially as the tissue temperature rises to 60 °C, and becomes instantaneous above 60 °C when protein denaturation occurs (Chu and Dupuy, 2014). Extreme heating (i.e., temperatures above 100 °C) progressively leads to vaporization of tissue water, initiation of tissue scarring, cavity formation, and carbonization. These effects must be avoided because they limit the extent of tissue injury by creating a heat trap and affect light penetration producing unwanted treatment outcomes (Nikfarjam, Muralidharan and Christophi, 2005).

In order to minimize these effects and achieve optimal tumor treatment, it is necessary to control the temperature both of the tissue and at the applicator's tip, and to constrain the desired temperature rise to safe oncologic margins (Laimer *et al.*, 2020). Advances in imaging techniques and the development of Magnetic Resonance Thermometry Imaging (MRTI) have opened the doors to promising approaches to improve LITT efficacy. Magnetic Resonance (MR) imaging is mostly used for tumor localization and targeting, and MRTI enables the visualization in real-time of the treatment effect. Hence, MRTI is able to provide a non-invasive multidimensional measurement of the temperature inside the human body, and inside the target organ and target tissue allowing the improvement of the therapy efficacy (Senneville *et al.*, 2007). LITT is especially well suited for MR guidance as the thin fiber-optic applicators do not create large susceptibility in the MR images (Odéen and Dennis L. Parker, 2019b).

Available commercial systems for MR-guided LITT exploit the proton resonance frequency shift (PRFS) as a method to extract temperature maps. In MRTI several parameters are showing

2

temperature-dependence (Odéen and Dennis L. Parker, 2019c). PRFS-based MR thermometry is the method used most often clinically thanks to linear temperature dependency for aqueous tissues, high sensitivity and tissue type independence (Ishihara *et al.*, 1995).

The main clinical challenges in PRFS-based MR thermometry are related to a lack of sensitivity in adipose tissues, respiratory motion, magnetic field drift, temperature-induced changes of tissue electric conductivity, and susceptibility changes (Winter *et al.*, 2016). B_0 field drift can result in substantial errors in phase difference maps when large gradients are applied, such as for the 3D imaging implementation and in Echo Planar Imaging (EPI) pulse sequences. The resonance frequency is very sensitive to changes in the local magnetic field because the PRFS method is based on measurements of small frequency changes. Magnetic field drift results in consistent temperature errors (e.g. apparent temperature change of up to 7 ℃/min which increase further over the scanning time (Bing *et al.*, 2016)), which can be corrected in the post-processing step (Odéen and Dennis L Parker, 2019; Parker, Payne and Odéen, 2022). On the other hand, artifacts in the images induced by local susceptibility changes may occur during thermal therapies thus interfering with the thermal damage map estimated by the MRTI. Susceptibility-related artifacts were observed during high-intensity focused ultrasound (HIFU) thermal therapy (McLean *et al.*, 2021),(Sprinkhuizen *et al.*, 2010). In these studies, susceptibility changes induced by temperature variation in adipose tissues cause dipole-structured artifacts leading to temperature errors of 15%. Similar artifacts were observed also during radiofrequency thermal therapy (Viallon *et al.*, 2010) and were associated with gas bubble formation in the electrode vicinity. The formation of gas bubbles produces magnetic susceptibility strong contrast and forms dipolar-structured artifacts corrupting PRFS-based MR thermometry. Recently, Munier et al. have found similar artifacts in the images during MR-guided LITT (Sean M. Munier, Liang, *et al.*, 2020). They performed 116 treatments for various intracranial procedures finding artifacts in 37% of the cases but the cause of signal artifact was considered unknown. Overall, artifact-related temperature errors strongly affect thermal damage estimation eventually invalidating the monitoring of LITT (Sean M. Munier, Desai, *et al.*, 2020).

In this work, artifacts appearing in MR Thermometry images during LITT and linked to magnetic field distortion related to susceptibility variations, are firstly shown during *in vivo* LITT in the liver and then characterized in both homogeneous and non-homogeneous tissue-mimicking phantoms. Gelatin phantoms and *ex vivo* porcine livers were used to understand the nature of artifacts, their extent, and the impact of misleading information associated with them. Firstly, a criterium for identifying the area and total volume of dipolar-shape regions and their evolution during the treatment was defined. Then, the temperature error consequent to susceptibility artifact formation was estimated with temperature-sensing needles providing temperature values used as a reference. As a final step, LITT was performed using temperature-based control strategy where the laser power was regulated based on temperature measurements, in order to control the effect on *ex vivo* tissue in an attempt to avoid artifact formation.

3

2   Materials

2.1 Magnetic Resonance Thermometry Imaging

In PRFS-based MR thermometry, the temperature maps are computed using a widely available gradient recalled echo (GRE)-type MRI pulse sequences. PRFS thermometry is based on the dependency of the local magnetic field of hydrogen atoms in water molecules, B_{local}, with temperature. The local magnetic field generally relies on the main magnetic field, B_0, volume magnetic susceptibility, χ_0, and shielding constant of the protons, σ_{total}. For aqueous tissues, since the shielding constant is approximately an order of magnitude larger than the magnetic susceptibility (Odéen and Dennis L Parker, 2019), a simplified equation describing the local magnetic field dependency only on B_0 and σ_{total} can be written as:

$$B_{local} \cong (1 - \sigma_{total})B_0 \tag{1}$$

The temperature dependence of σ_{total} causes B_{local} value to be changed under temperature variation. Hydrogen bonding between protons and the surrounding oxygen atoms on water molecules demonstrates linear temperature dependence, $\sigma_{total}(T) = \alpha T$, where α is the temperature-dependent chemical shift coefficient (ppm/°C). The direct proportionality between proton resonance frequency (PRF) and B_{local} with respect to the gyromagnetic ratio, γ, finally leads to PRF dependence with temperature. The change in PRF with temperature is observed in the phase of complex MRI image so that temperature maps of tissue can be created using:

$$\Delta T = (\varphi - \varphi_{REF}) / (\gamma \alpha B_0 TE) \tag{2}$$

where φ_{REF} is the baseline reference phase acquired before the temperature change, φ the phase image acquired while the temperature is changing, and TE is the echo time. By subtracting φ_{REF}, all the non-temperature-related contributions are eliminated, and the relative increase of temperature is calculated. In the end, the PRFS method is able to measure an induced temperature change. To convert it to absolute temperature the baseline temperature must be known and added to the calculated change.

 Equation 1 does not consider the χ_0 temperature dependence. Hence, its effect induces temperature errors smaller than 10% for the aqueous tissue (De Poorter, 1995). On the contrary, in adipose tissue the χ_0 temperature-dependence can cause magnetic field distortions leading to substantial dipole-structured errors in the thermal maps (Sprinkhuizen *et al.*, 2010), such errors may occur even with adequate fat signal suppression (Baron *et al.*, 2014). Additionally, previous studies demonstrated that gas bubbles produce magnetic susceptibility changes which induce dipole magnetic field disturbance artifacts in the MR images (Viallon *et al.*, 2010).

4

Susceptibility effects depend on the geometry and orientation of both the device delivering heating and the pattern of the temperature rise, relative to B_0 (Viallon *et al.*, 2010). When gas bubbles form during heating they often induce a lobe-butterflylike pattern, which is observable in the sagittal slice when the heating probe is inserted perpendicular to B_0. The pattern has a typical dipolar structure and therefore suggests localized susceptibility changes. Changes in the susceptibility distribution lead to magnetic field changes, which occur not only locally at the site of the susceptibility change, but also arise nonlocally in the surroundings of the susceptibility change. In static tissue, these magnetic susceptibility-effects are far overweighting all other competing sources of error discussed above.

2.2 Temperature-sensing needles

In this study, temperature-sensing needles based on optical fiber technology enabled multi-point temperature measurements (De Landro *et al.*, 2020). A chemically inert and small diameter (~155 µm) optic fiber containing fiber Bragg grating (FBGs) was used as a temperature reference. FBG is a periodic modulation of the refractive index in the fiber core, that reflects a particular wavelength (dependent on the period of the modulation), the Bragg wavelength λ_B, and transmits all others. FBG sensing principle is based on the fact that perturbations of temperature along the grating cause a shift $\Delta\lambda_B$ of the λ_B, following:

$$\Delta\lambda_B / \lambda_B = \beta\Delta T \tag{3}$$

where β ($°C^{-1}$) is the thermal sensitivity of the grating. As a result, FBG acts as a sensing point.

Moreover, a fiber with a chain of FBGs (also called an FBG array), each with different periodic modulation and related Bragg wavelength, is able to provide multi-point temperature measurements along the fiber. In this regard, the use of multiple fibers with FBG arrays allows the reconstruction of discrete 2D or 3D temperature maps (Morra *et al.*, 2020).

In our experiments, two custom-made arrays of 40 FBGs and one commercially-available array of 10 FBGs (FiSens GmbH, Braunschweig, Germany) were used. The custom-made arrays have grating lengths of 1.19 mm, and edge-to-edge distances of 0.01 mm (resulting spatial resolution is 1.2 mm, sensing length is 48 mm). The commercial arrays have 1 mm grating lengths and 1 mm edge-to-edge distances thus having a spatial resolution of 2 mm and a sensing length equal to 19 mm.

3 Methodology

3.1 Problem statement: in vivo LITT

In *vivo* experiments were performed which demonstrated the artifacts formation during porcine liver LITT providing then the necessity for the more precise investigation performed in this manuscript in tissue-mimicking phantoms. The study received full approval from the Institutional Ethical Committee of the Institute of Image-Guided Surgery of Strasbourg (Protocol 38.2015.01.118) and the French Ministry of Superior Education and Research (Project authorization APAFiS#19543-2019030112087889). It was conducted in compliance with French laws for animal use and care and according to the European Directive 2010/63. Pigs are housed in social group with an acclimatization period before experimentation, they receive standard piglet pellets and chew toys for enrichment. Anaesthesia is preceded by 24 hours of fasting. One male pig (Large White x Landrace x Pietrain, body weight 45 kg) was sedated in its pen with intramuscular injection of tiletamine+zolazepam 5-10 mg/kg (Zoletil 100®, Virbac France), and transferred to the operative room. Anaesthesia was induced by intravenous injection of propofol 2-4 mg/kg (Propovet®, Zoetis France) combined with rocuronium 1-2 mg/kg (Esmeron® MSD France) to allow endotracheal intubation and mechanical ventilation. Anaesthesia was maintained with 2% isoflurane (Isoflurin®, Axience France) inhaled in a mix of O_2/NO_2 50%/50% 2l/min. Body temperature, heart rate, oximetry and $EtCO_2$ were monitored to ensure the follow-up of the anaesthesia. Repeated injections of rocuronium and propofol were required to maintain muscle relaxation and sedation. Fentanyl 3-5 µg/kg IV (Fentadon ® Dechra France) was administered as a painkiller. Perfusion of NaCl 0.9% 10 ml/kg/h was continuously infused through the marginal ear vein. At the end of the procedure, the animal was sacrificed under general anaesthesia with an injection of pentobarbital 40 mg/kg IV (Euthoxin®, Osalia France).

LITT was performed with a 975 nm laser diode (LuOcean Mini 4, Lumics, Berlin, Germany), delivering the radiation to an MR-compatible fiber applicator with a 365 µm diameter (THORLABS, Dachau, Germany). The laser applicator was inserted using a carbon needle of 1.5 mm and placed perpendicular to B_0. The target locations were identified using pre-acquired MR images, considering liver lobes and surrounding vascular structures. A standard ultrasound (US)-guidance protocol using a curvilinear transducer (Acuson S3000 + 6C1 transducer, Siemens Healthineers) was used to guide and navigate the needles to the pre-defined location (Figure 1). An initial scan was performed to recognize intrahepatic anatomy, and a step-wise insertion of the needle with multiple checkpoints was carried out under a single apnea. The final position of the needles was controlled using MR images. After laser applicator placement, the laser system was set to deliver power at 2 W for 10 minutes. The temperature was measured using MRTI. Data were acquired with a prototype 3D segmented EPI sequence in the plane housing the laser applicator. Images were respiratory-triggered in the expiratory phase. The following parameters were used: field of view 294 mm x 294 mm, in-plane resolution 1.4 mm x 2.8 mm, reconstructed resolution 1.4 mm x 1.4 mm, slice thickness 3 mm, 12 slices, TE/TR=12 ms/22 ms, flip angle 10°, EPI factor

6

11, GRAPPA 2, temporal resolution 1.78 s, 400 repetitions, leading to an overall acquisition time of ~12 minutes. The cooling phase was monitored for ~3 minutes.
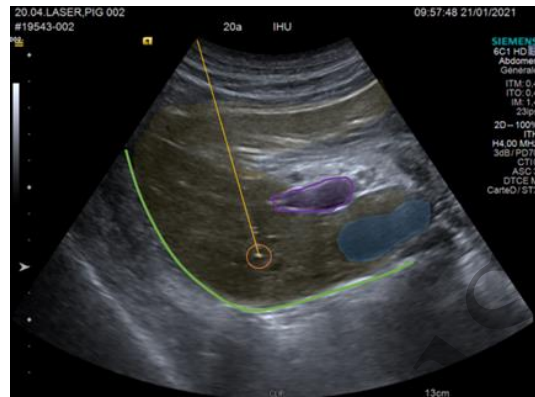

Figure 1: Needle trajectory (yellow line) and tip (orange circle), main portal vein (purple), inferior vena cava (blue), diaphragm (green), and liver (yellow).

The 3D sequence provided magnitude and phase images and the latter were used to obtain the thermal images using equation 2 with baseline acquisition of 30 s, α=0.0094 ppm/ °C; γ=42.58 MHz/T; B_0 =1.5 T; TE =13 ms. The B_0 drift was then corrected in post-processing with zero-order baseline correction selecting a reference area in the target far from the ablation region and subtracting the effect of the non-temperature related field drift (Viallon *et al.*, 2010).

3.2 Artifacts characterization: tissue mimicking phantoms LITT

3.2.1 Tissue mimicking phantoms

For the characterization of the susceptibility artifacts, the first series of experiments were performed in a porcine-based gelatin phantom, which holds the advantage of being a homogeneous and reproducible medium. According to the provider's instruction, the gelatin powder (porcine gelatin powder, 200 bloom, LOUIS FRANCOIS, France) was stirred with tap water (10 g/100 mL) for about 5 hours until a homogeneous solution was obtained. Then, the solution was poured into boiling water. After cooling down to room temperature, the solution was stored in the fridge (8 °C) for 6 days in an MR-compatible plastic container (biggest diameter 15 cm, base diameter 13.5 cm, and height 7 cm).

The second series of experiments were performed on *ex vivo* porcine livers mounted in gelatin support (Figure 2a). In order to comply with the requirements of reduction and alternative methods, the livers used in this work were harvested from pigs previously utilized in other studies, at the Institute of Image-guided Surgery of Strasbourg (IHU Strasbourg), France. Animals were manipulated following all the recommendations available in the Guide for the Care and Use of Laboratory Animals of the National Institutes of Health, and in full compliance with French laws for animal use and care, and with the directives of the European Community Council

7

(2010/63/EU), and with the 3Rs principles (Replacement, Refinement, and Reduction), and developed in congruence with the best welfare animal conditions. Two livers were procured from animals' breed Sus Scrofa Domesticus, ssp. Large White, immediately after euthanasia by a hepatobiliary surgeon, following the "standard" technique (Makowka *et al.*, 1988). Then, the organs were stored in the fridge (8 °C) for 8 hours until the mounting step. Liver tissues were mounted in gelatin to facilitate the control of needles placement in it. The four tissue lobes were separated and mounted on 3 cm of inferior gelatin block previously prepared and in a solid state. Additional gelatin was then poured while in the liquid state until completely covering the entire sample. The final organ-in-gelatin system was stored in the fridge after cooling at room temperature.

3.2.2 Experimental strategy

The artifact was characterized in both gelatin-phantom and *ex vivo* porcine livers in two ways: (i) analysis of dimensions measuring the area and total volume of error regions and their evolution during the treatment; and (ii) comparison with temperature reference provided by three temperature sensing needles placed in the target.

Therefore, the FBG arrays were embedded in an MRI-compatible carbon needle of an external diameter of 1 mm for visualization in the MR images and positioning control. The temperature-sensing needles, finally consisting of 48 mm (40 FBGs array) and 19 mm (10 FBGs array) sensing length from the needle tip, were calibrated in a certified thermostatic calibrator (Giussani Quartz, operative field from -40 °C to 125 °C) in the temperature range 20 °C - 80 °C, with a step of 10 °C. The laser system (same as the *in vivo* case) was set to deliver power at 0.5 W and 2 W for 5 minutes, for comparison of the two cases of artifacts' absence and presence, respectively. Preliminary experiments showed artifacts formation when a power higher than 2 W was set.

A three-dimensional (3D) printed frame in polylactic acid was fabricated to control the relative position of the temperature-sensing needles and laser applicator in the targets as shown in Figure 2b-c. The 3D-printed object was designed to be placed on the top of the plastic phantom container and consisted of 55 mm deep holes allowing the needles to keep a relative parallel position inside the phantoms. The pattern consisting of several holes offered a wide range of possible arrangements for the needles. The final experimental configuration is shown in Figure 2b. The 2 mm diameter central hole was used for the laser applicator needle, whereas the three temperature sensing needles (Figure 2d) were all placed on one side with a relative distance of 0.5 cm. The 40-FBGs needles were placed closer because of the higher temperature gradient in the laser applicator vicinity. The farthest one consisting of 10-FBGs, was inserted 1.5 cm far from the laser source. Indeed, the preliminary analysis demonstrated for the artifact a double-lobe symmetric shape with respect to the laser applicator with total maximum extension in the sagittal plane of ~ 2.5 cm along head-foot line. The interrogation system Micron Optics si155 (Micron Optics, Atlanta, USA) was used to acquire data from sensing needles with 10 Hz sampling rate.

8

The final setup is showed in Figure 2e. Phantom in an open plastic box was placed with the 3D-printed frame in the 1.5 T MRI scanner (MAGNETOM Aera, Siemens Healthineers, Erlangen, Germany). MR images were acquired with a flexible 4-channel coil and the spine coil integrated into the MR bed. The flexible coil was positioned for signal reception on the upper side of the entire system as shown in the figure. Before each thermal ablation, anatomical images were acquired to check laser and temperature sensing needle positions using T1-weighted 3D volumetric interpolated breath-hold examination (VIBE) sequence with the following parameters: field of view 300 mm x 300 mm, in-plane resolution 1.2 mm x 1.2 mm, slice thickness 1.5 mm, 56 or 64 slices, TE/TR=1.98 ms/4.69 ms, flip angle 10°, fat saturation, GRAPPA 2, TA=37 s or 39 s. The T1-weighted VIBE orientation was chosen to be axial or sagittal, according to needles and laser positioning in the target.

MRTI data were acquired with a prototype 3D segmented EPI sequence in the axial and sagittal orientation for a complementary analysis of the artifact behavior. Slices were always placed parallel to the laser applicator and sensing needles. Four ablations were performed for each laser power value, two in the sagittal and two in the axial orientation. The following parameters were used: field of view 300 mm x 300 mm, in-plane resolution 1.4 mm x 2.8 mm, reconstructed resolution 1.4 mm x 1.4 mm, slice thickness 3 mm, 10 slices, TE/TR=13 ms/24 ms, flip angle 10°, EPI factor 7, temporal resolution 3.62 s, 135 repetitions, leading to an overall acquisition time of ~8 minutes. The cooling phase was monitored for ~3 minutes.
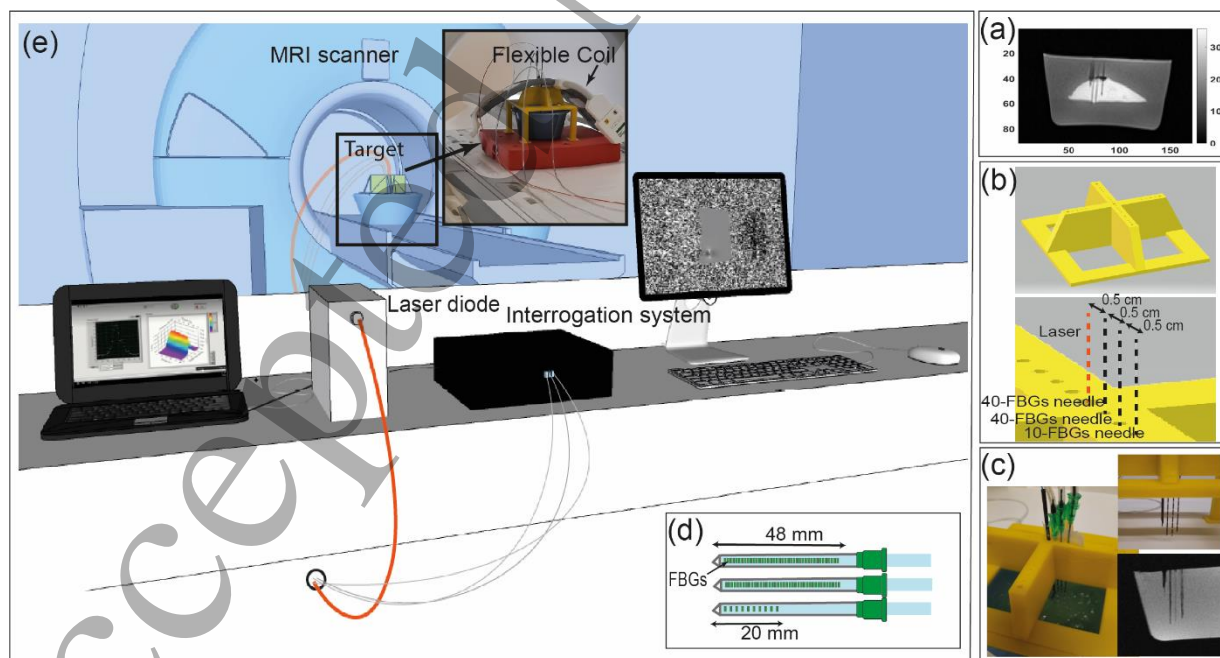

Figure 2: (a) *Ex vivo* **liver mounted in gelatin. (b) 3D printed object used to place sensing needles and laser applicator. The central hole housed the laser fiber, whereas the three temperature sensing needles were placed**

9

with 0.5 cm distance from each other. (c) Detail of needles inserted in the 3D-printed object which allows them to keep a relative parallel position inside the target. (d) The two 40-FBGs arrays and the 10-FBGs array embedded inside fiber-carbon needles. (e) Final Experimental setup. The target scanned in the MR system consisted of a 3D printed object placed on the top of the plastic container including tissue phantoms. A flexible coil was positioned for signal reception on the upper side of the entire system. A 975 nm laser diode delivered the radiation to an MR-compatible fiber applicator (orange) which was inserted in the phantoms through the 3D-printed object. Micron Optic interrogator was used to acquire the signal coming from temperature sensing needles (grey) also inserted using the 3D-printed object.

3.2.3 MRT images analysis

Temperature images were obtained using equation 2 and B_0 drift was corrected in post-processing as described above. To perform the analysis of the dimensions, the MRTI images were segmented to detect the area of interest corresponding to the susceptibility artifact in both axial and sagittal planes. For this purpose, regions demonstrating underestimation of temperature were defined as regions of errors due to susceptibility change. Temperature maps were firstly masked out to remove the temperature values in pixels with low MRI magnitude signals using a threshold of 0.3 times the maximum amplitude. Then, pixels showing temperature values < -1 °C were labeled as susceptibility artifacts after applying a median filter with a 4-by-4 window. The second step, providing temperature error estimation using temperature sensing needles data, was implemented only for the experiments carried out in the sagittal plane. The artifact appears, indeed, to be mainly distributed along that orientation as demonstrated in the analysis of the dimensions (see results section). This could be ascribed to the choice of placing the laser applicator perpendicular to B_0 (Viallon *et al.*, 2010).

To perform the comparison between MRTI and FBGs, the two datasets were temporally synchronized by subsampling the signals acquired by FBGs at the same frequency of the MR acquisitions. Then, FBG sensor – MRTI pixel spatial matching was performed in a single slice which was selected according to the needle positions. Specifically, the slice showing needle holes was supposed to house FBG sensors and was chosen for the comparison analysis. The pixels were selected as close as possible to each sensing needle but outside the fiber tip artifact. To find the match sensor-pixel, temperature evolutions were compared until accordance for three sensors-pixels (one for each needle) in the area not affected by susceptibility error. Starting from the selected pixel-sensor match, the temperature evolution in the artifact area was also juxtaposed by recursively selecting the pixel-sensor combination knowing edge-to-edge distance and length of FBG, and pixel dimension.

In the gelatin-based phantom, a quantitative estimation of the artifact-induced temperature error was possible. This analysis was performed in the sagittal direction and for the second needle line which is more descriptive of the artifact error since the line of pixels includes both temperature values inside and outside the susceptibility artifacts area. Starting from the pixel-sensor match, an absolute error was measured as the difference between the temperature values measured by MRTI and FBGs along the second needle line.

10

Temperature values measured from the 90 FBGs sensors were also used to reconstruct an alternative and complementary temperature map in the area of the artifact.

3.3 Possible solution to avoid artifacts: temperature-based control LITT

Additionally, temperature-controlled LITT was performed to avoid any artifact formation in *ex vivo* porcine livers. From previous experiences (see results section for *ex vivo* liver), it is, indeed, clear that the occurrence of unwanted treatment outcomes due to extreme temperature values may lead to susceptibility artifacts in organs. Since temperature errors due to artifacts make MRTI measurements not reliable, LITT was controlled using FBGs temperature measurements. The experiments were carried out with the same experimental setup in Figure 2e. A dedicated 3D-printed system was used allowing for a laser applicator-sensing needle relative distance of 0.2 cm (Fig. 3a). The final configuration provides the placement of one single needle with 40-FBGs, and the temperature values measured from the sensing needle were used to control laser power via a custom-made LabVIEW program. Temperature-controlled LITT is performed in three stages (Fig. 3b): (i) linear phase, (ii) proportional-integral-derivative (PID) control, and (iii) cooling phase. At the beginning, (i) the laser power is linearly increased until the maximum temperature measured by MRTI (temperature in the voxel closest to the applicator tip) reaches $T_{set,MRTI}$=35-40 °C over the initial temperature. Then, (ii) the temperature measured by FBG at this moment ($T_{FBG,con}$) is maintained stable using PID control for steady-state time duration or until maximum MRTI temperature change (T_{max}) will reach 50 °C. Finally, (c) the laser is switched off and cooling temperature is measured during 60 s.
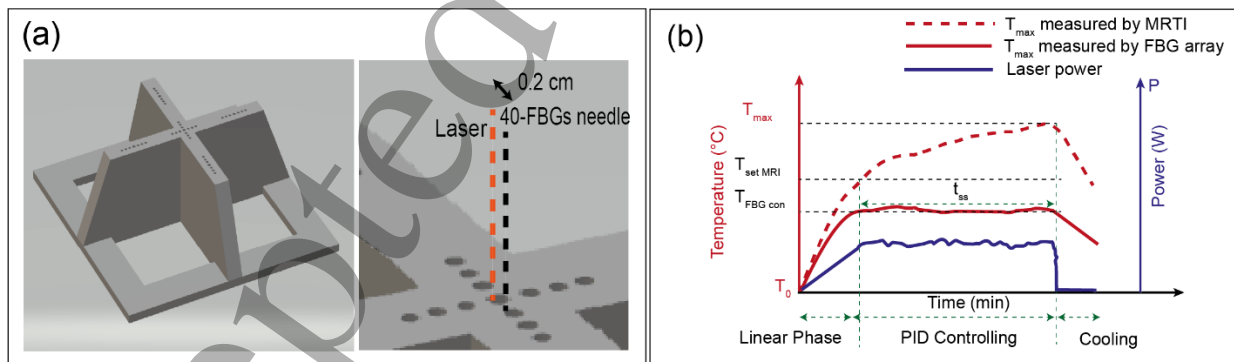

Figure 3: (a) 3D-printed object and configuration of laser and sensing needle used in the PID control experimental step. (b) Experimental strategy for LITT control implementation.

MRTI data were acquired with a prototype 3D segmented EPI sequence in the sagittal orientation to have slices parallel to the laser applicator and temperature sensing needles. The following parameters were used: field of view 300 mm x 300 mm, in-plane resolution 1.4 mm x 2.8 mm, reconstructed resolution 1.4 mm x 1.4 mm, slice thickness 3 mm, 10 slices, TE/TR=13 ms/24 ms, flip angle 10°, EPI factor 7, 5 baseline averages to reach equilibrium magnetization, temporal

11

resolution 3.62 s, 300 measurements leading to total acquisition time of ~20 minutes. Temperature maps were obtained again as explained in section 2.1. Also, temperature values were displayed in real-time using Certis Solution (CERTIS Therapeutics, Pessac, France) for checking artifact appearance during LITT implementation and verifying the performance of the temperature-based control approach.

4 Results

4.1 In vivo LITT

An example of susceptibility artifacts appearing during *in vivo* LITT in liver is shown in Figure 4. Temperature maps acquired for the slice intersecting the LITT applicator tip are reported along the time. The temperature value < -1 °C and > 1 °C are shown for visibility. Artifacts appear with a double-lobe shape of negative temperature increase in blue with black margins. The real-time monitoring of the induced temperature is, indeed, strongly affected by the artifact's appearance. These results have encouraged the investigation of the artifact behavior in tissue-mimicking phantoms described in the work.
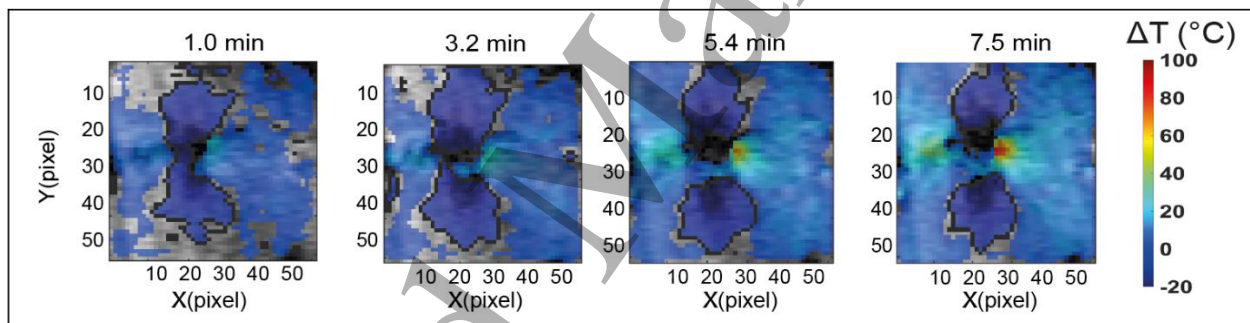

Figure 4: Temperature maps showing susceptibility artifact for LITT at 2 W in *in vivo* liver during time. Artifacts are visible as negative temperature variation in blue and are highlighted with black margins in the slice intersecting the LITT applicator tip.

4.2 Tissue mimicking phantoms LITT

4.2.1 Artifact dimensions analysis in gelatin

Temperature maps measured in the 10 slices for both axial and sagittal orientations are reported for the 0.5 W (Figure 5a) and 2 W (Figure 5b) cases. Time instant associated with maximum temperature increase (~5.5 minutes) was chosen for the visualization. In the experiment performed with low power, temperature maps are not affected by artifacts and the maximum temperature increase is 23 °C.

When a power of 2 W is set, artifacts appear with a double-lobe shape of negative temperature increase also in this case (Figure 5b). Again, the areas of susceptibility error are visible as negative temperature variation in blue. 3D rendering of the artifact shape in Figure 5b helps to understand

12

the reason why in the sagittal orientation (in green) a double-lobe is clearly visible compared to the axial view (in blue). Therefore, the artifact shape allows better visualization and characterization in the sagittal view compared to the axial one. In the 2 W case, the maximum temperature reached cannot be estimated using MRTI values because of not-reliable temperature measurements in the proximity of the artifact laser applicator tip. Although in this analysis we labeled the negative temperature increase as error regions, in the area closest to the laser tip a magnitude signal lost due to effects induced by laser treatment in the target is measured. This causes misleading temperature values in the laser tip proximity as well. Considering a maximum temperature of 35 °C estimated by FBGs at 0.5 cm, we can consider a peak temperature of around 100 °C which is reasonable assuming the boiling temperature of the water contained in the gelatin.

No effect is visible in the gelatin by comparing VIBE images acquired before and after LITT performed at 0.5 W (Figure 6a). Considering therapy outcomes when the higher power is set (Figure 6b), artifacts' appearance can be related to susceptibility change following bubble formations. Gas bubbles are indeed generated at the laser tip during LITT, as clearly visible in the series of US images in Figure 6c. The red arrow is indicating the laser applicator whereas the white one is showing the area of ablation which increases during the treatment. Gas bubbles suddenly appear close to the tip then they migrate following the direction of the laser applicator (Khokhlova *et al.*, 2009), and accumulate on the upper side of the ablated zone when the laser is switched off. The second bigger hole in the images is caused by the carbon-fiber needle used to place the laser applicator. When the needle is retracted, the track is remaining in the gelatin and the laser applicator is moving further during the ablation. Finally, the bubbles appear in the MR images as circular dark regions (inside the black circle in Figure 6b). The phase difference that appeared as the negative increase of temperature was likely due to the difference in magnetic susceptibility of the gel and the gas in the bubble.

The results of the dimension analysis are reported in Figure 7. The time evolution of the area of the artifact for the 10 slices is reported for both axial (Fig. 7a) and sagittal (Fig. 7b) directions. In the sagittal case, the area demonstrates a temporal evolution similar to the temperature trend, with the highest value around 5.5 minutes when the temperature is also maximum. Also, in a few slices it decreases when the laser is switched off.
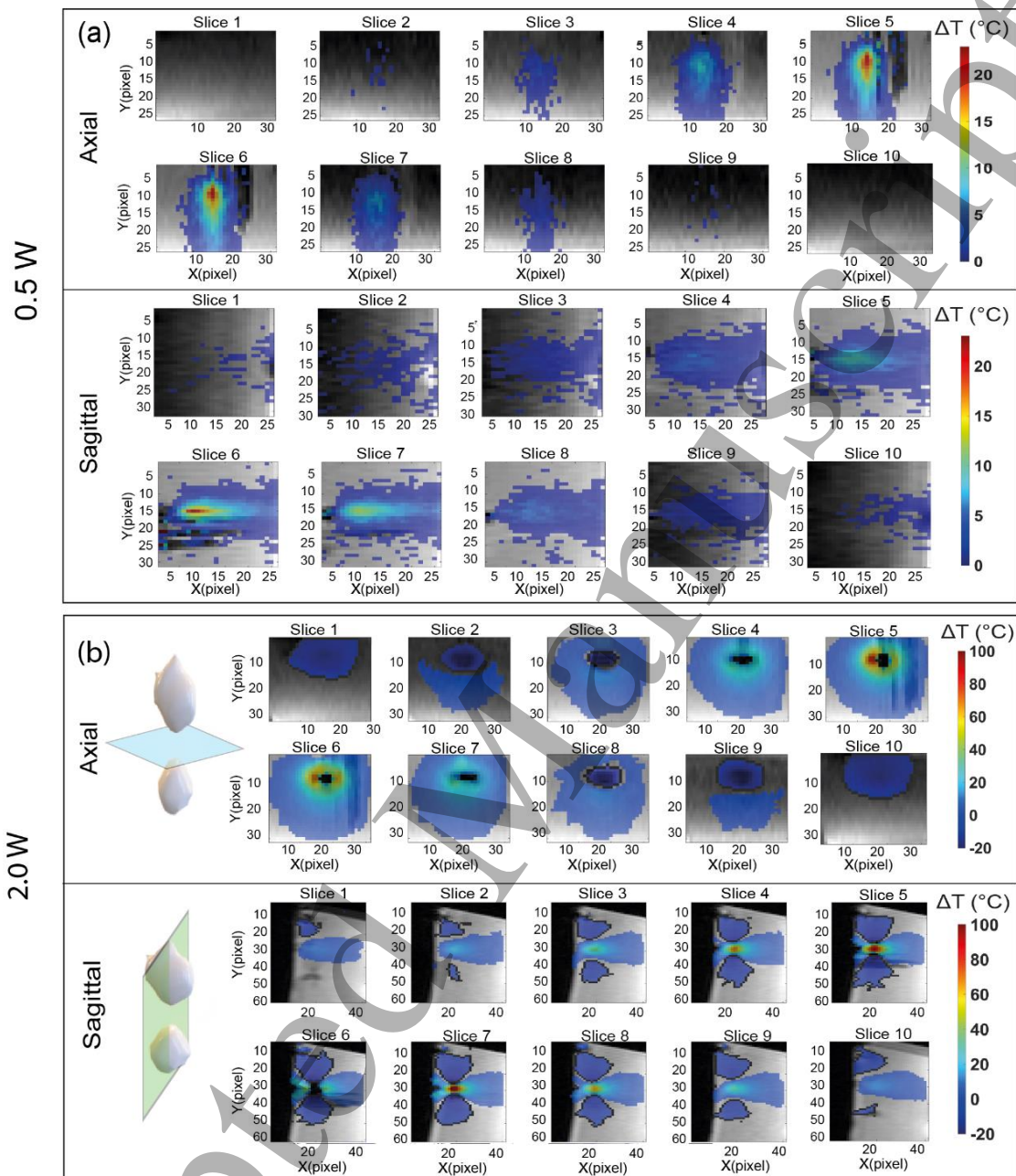
Figure 5: (a) Temperature maps for 0.5 W in the axial and sagittal planes, after 5.5 minutes from the MRTI acquisition start. (b) Temperature maps and 3D rendering of susceptibility artifact for LITT at 2W in gelatin in axial and sagittal orientations. Artifacts are visible as negative temperature variations in blue and are highlighted with black margins in all the 10 slices.
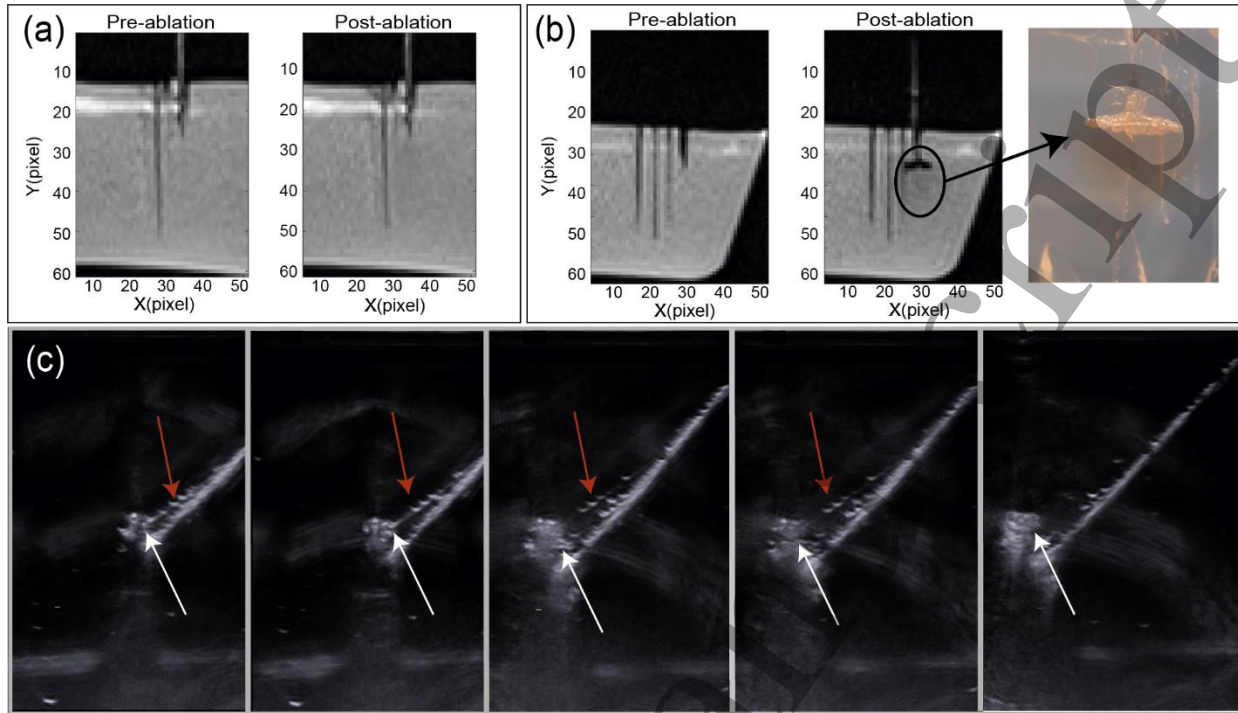
14

Figure 6: Therapy outcomes for (a) 0.5 W and (b) 2 W. Considering the observed results, the signal artifact can be related to gas bubbles formation in the gelatin when the higher laser power is set. (c) US images acquired during LITT in gelatin showing bubbles formation. The white arrow is indicating the area of ablation and the bubbles forming at the laser tip whereas the red arrow is showing the laser applicator.

In the axial direction, the behavior is different. Its evolution follows the temperature one in the external slices (Slice 1 and Slice 10) where the artifact shows the maximum dimension, whereas in Slice 5 the area is zero in accordance with its shape (see Figure 5b). The time evolution of the area for the axial plane shows an overall drop during ablation of 2-3-7-8 slices at the expanse of the external ones where the area increases until the laser was turned off (see also Figure 7c). On the other hand, in the sagittal case (Figure 7d), the maximum area along the time is always found in Slice 7 and a consistent drop of the artifact dimension is not estimated in the central slices during the cooling phase. The dimensions analysis demonstrates that the artifact shape is quite symmetric with respect to the laser tip and confirms that the artifact is mainly distributed in the sagittal orientation when the laser applicator is inserted perpendicular to the main magnetic field. In the gelatin, the two performed experiments exhibit similar trends for the susceptibility artifacts in both directions (Figure 7e,f).

Maximum values for artifact area were measured to be 9.20 cm^2 and 6.17 cm^2 in the sagittal and axial planes, respectively. Maximum total volume was also measured knowing the slice thickness and it was found to be 117.7 cm^3 and 162.2 cm^3 in the two tests performed in the sagittal direction, and 56.9 cm^3 and 52.3 cm^3 in the axial case. Considering that the estimated volume of the ablated zone using the VIBE sequence was 15.9±4.3 cm^3, in the sagittal case, the artifact may affect a volume more than 8 times bigger than the volume of interest.
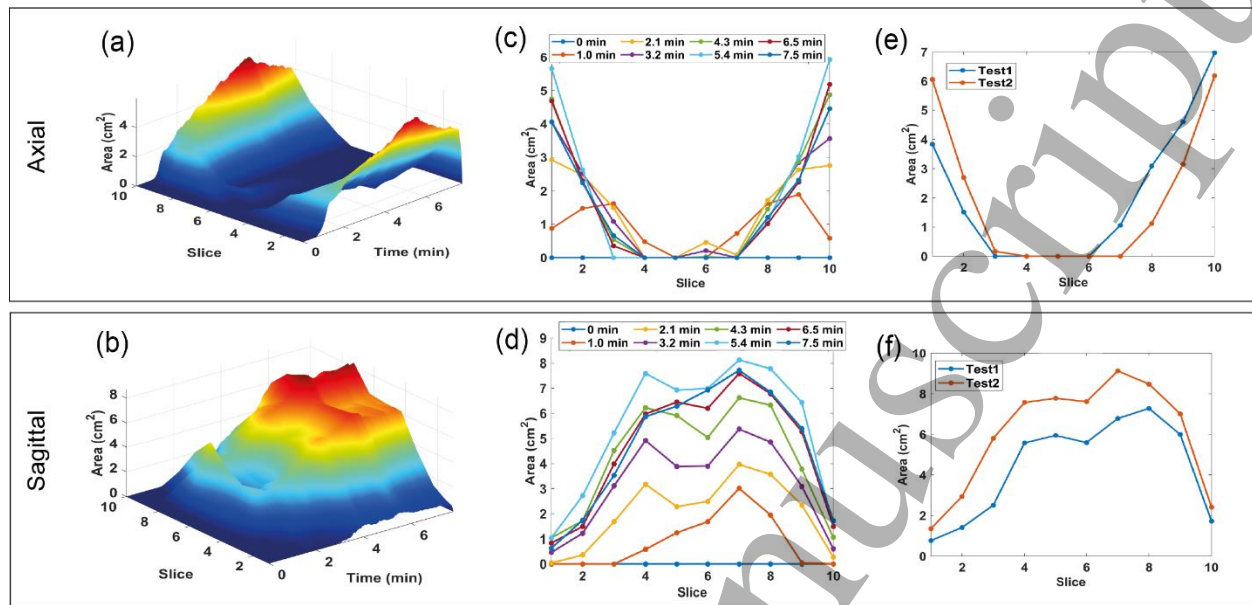
15

Figure 7: Analysis of dimensions of susceptibility artifacts in gelatin. Temporal evolution of the area of artifact in cm² in the 10 slices of (a) axial and (b) sagittal plane. Extracted area of artifact in the 10 slices for the experiments performed in the (c) axial and (d) sagittal plane. Values are calculated in seven temporal instants. Area in the 10 slices measured at the instant of maximum artifact dimensions in two tests for the (e) axial and (f) sagittal plane.

3.2.2 *Temperature error estimation in gelatin*

Temperature evolution measured with MRTI (blue) and FBG (orange) in 6 pixels is reported in Figure 8a. The 6 selected pixels positions are presented in Slice 5 at ~5.5 minutes. The first three pixels were chosen in the region far from the artifact (~ 15 mm far from the laser tip along the *x*-axis) and show good agreement overall. By comparing the signals acquired with both measurement systems, in all 6 pixels the MRTI signal exhibits more noise. On the other hand, FBG signal shows consistent and comparable noise when a slow increase of temperature is estimated (Point 3). In the area closer to the laser tip, although the temperature values are >-1 °C, a measurement mismatch is found because of the signal loss (see Point 4). In Point 5, a negative temperature shift is observable until 4 min of ablation, then the temperature increases overcoming the FBG value. This behavior indicates that the artifact was formed in that region but then moved. Considering Point 6, a negative temperature value is calculated during the whole ablation test because of susceptibility artifact presence.

For the quantitative estimation of the temperature error, the temporal evolution of the absolute error was obtained as average and uncertainty among the pixels belonging to three separated areas: -*Error_NoArtifact* (orange circle in Figure 8b): pixels belonging to this area show consistent temperature increase resulting in high absolute error due to low magnitude signal after 1.5 min from LITT started. Hence, when the needles are placed in the gelatin, the material undergoes

16

structural lesions causing signal loss and consequent temperature error in the area close to the insertion point. Such error does not rely on susceptibility artifacts.

-*Error_Artifact* (green circle in Figure 8b): pixels belonging to this area show a negative increase of temperature which causes negative absolute errors associated with susceptibility artifacts.

-*NoError* (blue circle in Figure 8b): pixels far from error areas experiencing a narrow absolute error.

Despite the high variation among the pixels, the behavior in time of the absolute error for each area is similar. Also, Figure 8c compares the absolute error along the entire pixel line in the two tests and for several time instants showing a similar trend. The three areas are again distinguishable (see the circles of different colors) and the absolute error shows a negative Gaussian profile in the *Error_Artifact* area where the highest value is measured. Furthermore, if in the *Error_Artifact* area the error increases during the ablation to then decrease during the cooling phase, in the *Error_NoArtifact* area for the Test1 it keeps almost the same values.

The maximum value of absolute error in the three areas after 5.5 min of LITT gave for the two tests:

-*Error_NoArtifact*: 23.9 °C and 19.7 °C

-*Error_Artifact*: 49.7 °C and 64.4 °C

-*NoError*: 1.9 °C and 2.8 °C

These results demonstrate a substantial error where the susceptibility artifact is found. Such error may consistently affect thermal damage estimation since it influences a significant portion of the ablation area in the sagittal plane, also including ablation margins. A lower error is measured in the area not-affected by artifacts and far from the applicator tip. This can be also associated with the lower increase of temperature and smaller temperature gradient experienced by the gelatin.

The temperature map obtained by interpolating all the 90 FBGs sensors at 5.5 min is shown in Figure 8d (see the bottom image with a yellow border). The three temperature sensing needles, represented with red lines in the interpolated map and with red pixels in the MRTI image, guarantee a good temperature reconstruction limited to the area housing the optical sensors.
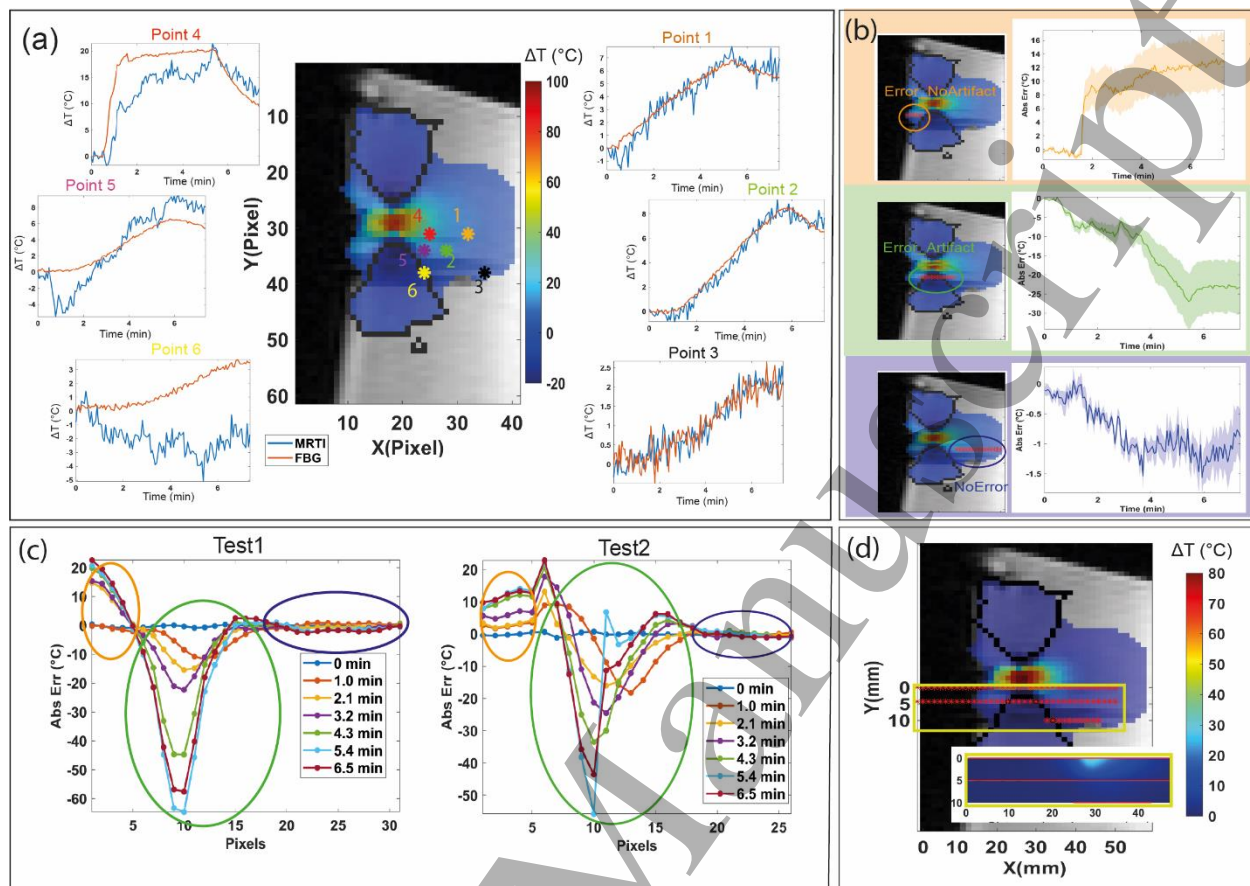
17

Figure 8: Comparison of MRTI with temperature measured by sensors. (a) Temperature evolution acquired with FBG (orange) and MRTI (blue) in 6 pixels. The position of the pixels is also reported considering slice 5 at 5.5 min. (b) Quantitative comparison of MRTI with temperature measured by FBGs. The temporal evolution of the absolute error was obtained as average and uncertainty among the pixels belonging to Error_NoArtifacts (orange circle), Error_Artifact (green circle), and NoError (blue circle) areas. (c) Absolute error along the line for several instants in Test1 and Test2. The pixels belonging to the three areas are highlighted with a orange circle for Error_Noartifact, a green circle for Error_Artifact, and a blue circle for NoError. (d) Temperature map implemented by interpolating the temperature values from the 90 FBGs sensors (bottom image with yellow border). The sensors' positions are also shown in the thermal map obtained with MRTI (red spots) and characterized by susceptibility artifact

3.2.3 Artifact dimensions analysis in ex vivo liver

For the tests performed in the ex vivo organ, only qualitative analysis was implemented for both artifact dimensions and temperature error estimation. Indeed, tissue inhomogeneities caused poor repeatability among tests and hard identification of unique behavior. When 0.5 W is used, as previously observed for the gelatin-phantom, liver temperature maps are not affected by artifacts and the maximum temperature increase is ~35 °C. On the other hand, when a higher power of 2 W is set, artifacts appear, but their shape is not so clear and definite because of tissue inhomogeneities. Temperature maps acquired in one test are shown in Figure 9a, and b for axial and sagittal case, respectively, and for one slice along the time. Bubbles are again formed in the tissue but they can follow different paths in the tissue according to tissue texture and

18

vascularization in the target region. Such structural dependence leads to a not-unique artifact shape in time by comparing the tests performed with 2 W in *ex vivo* livers. Nevertheless, the general trend looks similar to the gelatin-phantom case: Figure 9c shows that during the ablation the area increases in the external slices whereas in the zone closest to the laser tip (Slice 6-8) it drops. This time, the artifact dimension starts decreasing also in the external slices after 3 minutes of ablation, probably because of bubbles motion in regions further from the scanned volume. Concerning the sagittal case, a double-lobe of negative temperature shift is visible in the first steps of the ablation, then one region is more affected by susceptibility error. Figure 9d shows how after 2 min (yellow curve) the artifact shifts to the right and starts decreasing after 3 minutes of ablation as in the axial case. A spatial symmetry is less evident in this case.
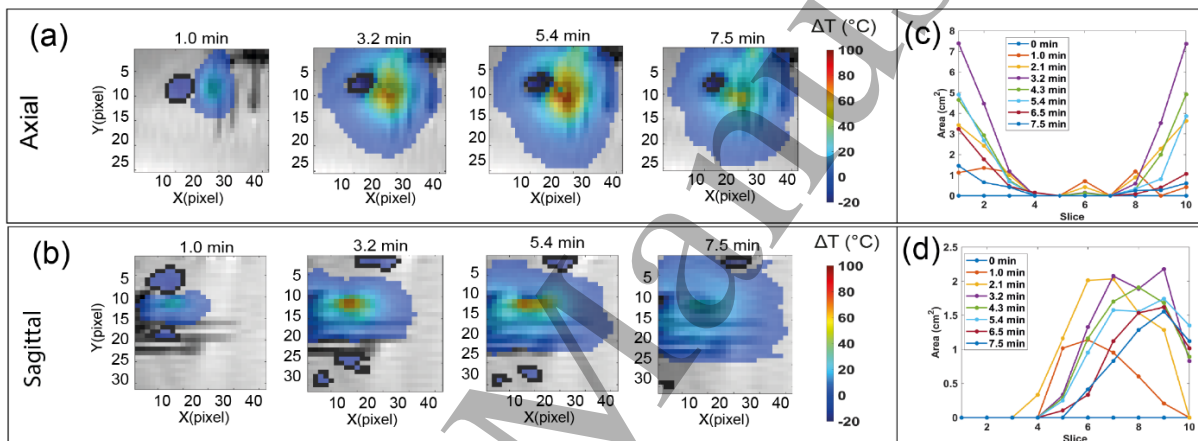

Figure 9: Temperature maps for 2W ablation in (a) axial and (b) sagittal planes in Slice 6 during *ex vivo* liver ablation. Extracted area of artifact in the 10 slices for the experiments performed in the (c) axial and (d) sagittal plane. Values are calculated in 8 temporal instants.

Bubbles formation in liver during LITT is shown in Figure 10a, whereas therapy outcomes are in Figure 10b-c. When a 0.5 W power is set, no carbonization or vaporization effects are produced in the tissue leading absence of bubbles and artifacts appearance. On the other hand, 2 W laser power induces unwanted treatment outcomes which also affect the temperature monitoring abilities of MRTI. The area of carbonization appears in the VIBE images as a black region (inside the black circle in Figure 10b).
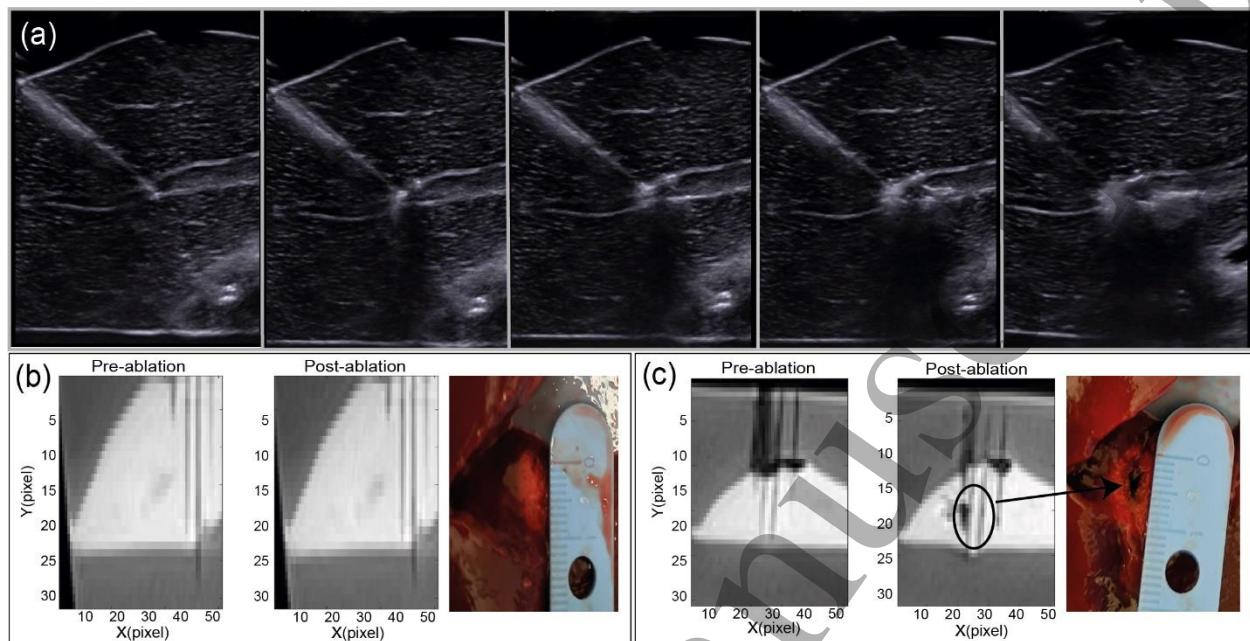
Figure 10: (a) US images in one of the tests. Bubbles are formed in the laser tip to then follow paths linkable to tissue structure and vessels. Therapy outcomes for (b) 0.5 W and (c) 2 W. Considering the results observed, the signal artifact is generated when vaporization and carbonization effects on tissue occur.

3.3.2 *Temperature error estimation in ex vivo liver*

Temperature evolution measured with MRTI (blue) and FBG (orange) in 6 pixels is reported in Figure 11a. The 6 pixels' positions are shown in slice 5 at 1.7 minutes. Pixels far from the artifact (~ 15 mm far from the laser tip along the x-axis) show better agreement (Points 1-2-4) overall. Points 3-6 belonging to the third sensing needle are both found in the artifact region and exhibit a negative temperature shift up to 6 min instant. In the area closer to the laser tip, the magnitude signal experiences reduced loss compared to the gelatin case (see Point 4). Hence, in the liver, such signal loss is mainly related to tissue carbonization and vaporization which is a spatially confined effect compared to melt or corrupted gelatin. Also, in the liver case, the result of interpolation using 90 sensing points provided by FBGs arrays demonstrate the potential of such technology in integrating temperature info provided by MRTI (bottom image with a yellow border in Figure 11b).
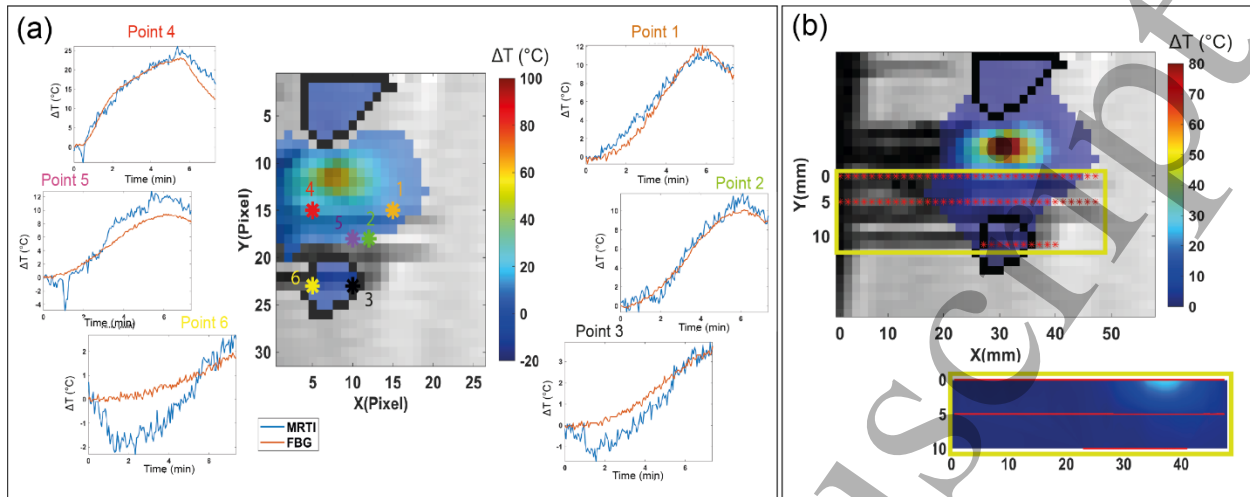
Figure 11: Comparison with fiber optic sensors. (a) Temperature evolution acquired with FBG (blue) and MRTI (orange) in 6 pixels. The position of the pixels is also reported considering slice 5 at 1.7 minutes. (b) Temperature map implemented by interpolating the temperature values from the 90 FBGs sensors (bottom image with yellow border). The sensor's positions are also shown in the thermal map obtained with MRTI (red spots) and characterized by susceptibility artifact.

4.3 *Temperature-based control LITT*

Temperature maps measured when LITT was performed using a temperature-controlled approach are reported in Figure 12a. The starting linear phase combined with the PID temperature control strategy guaranteed the absence of artifact during the liver interstitial ablation. Figure 12b shows the power delivered by the laser fiber during one temperature-based control experiment. The evolution in time of the controlled temperature is also reported with the maximum temperature measured by MRTI at the laser tip. The calculated temperature increase corresponds to absolute temperature in the range of 53-66 °C for the tissue considering the starting temperature of 18 °C in the *ex vivo* liver which causes thermal damage after a few minutes of treatment. Specifically, for temperature >60 °C the damage is instantaneous. The thermal damage induced after the treatment with a temperature-controlled strategy is visible in the MR images obtained after the ablation treatment with VIBE sequence (encircled area in Figure 12c).
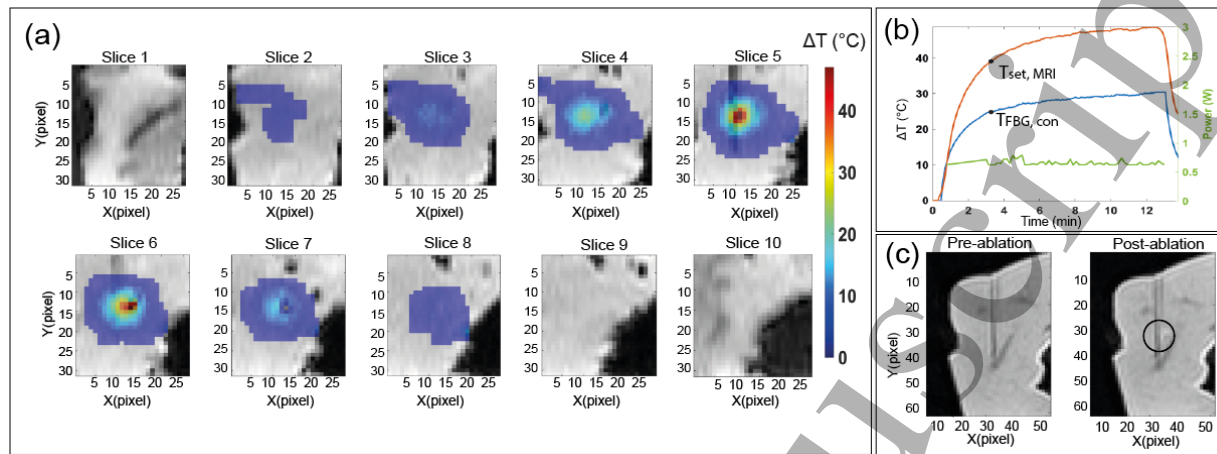
21

Figure 12: Temperature-controlled experiments results. (a) Thermal maps acquired in the 10 slices at minute 12 showing the absence of susceptibility artifacts. (b) Temperature measured by FBG and controlled with the implemented strategy (in red), consequent evolution of maximum temperature measured with MRTI (in blue) close to laser tip and power used during the temperature-controlled experiment (in green). (c) Therapy outcome for power-controlled LITT.

4   Discussion

This analysis confirmed the appearance of susceptibility artifacts during MR-guided LITT. A recent study pointed out the presence of MRTI artifacts affecting thermal damage estimation during *in vivo* LA treatments and observed that the increased power was associated with an increased incidence of artifact (Sean M. Munier, Liang, *et al.*, 2020). In our case, either in the *in vivo* liver and in tissue-mimicking phantoms (porcine-based gelatin and *ex vivo* liver), the 2W laser power produced the double-lobe shape of negative temperature increase associated with susceptibility variation. Our investigation in tissue-mimicking phantoms linked the artifact appearance with gas bubble formation (also seen with US images and outcome in the gelatin) and with unwanted treatment effects which produce magnetic susceptibility changes as already noted in (Viallon *et al.*, 2010).

Viallon et al. performed US/MR monitoring of radiofrequency thermal therapy and showed that gas bubbles and dipolar-structured artifacts occurred, and progressively evolved synchronously in PRFS-based MRTI. Although the authors distinguished a four-lobe butterflylike pattern in the sagittal slice showing both negative and positive temperature values, in this work only the regions demonstrating underestimation of temperature were defined as regions of errors due to susceptibility change. This is because if a negative increase of temperature is not expected during thermal ablation, the positive temperature increase cannot easily be distinguished as a measurement error. Future studies should consider the total region of the four-lobe butterflylike pattern as the region of error causing misleading temperature values. Focusing on negative lobes, the analysis of the artifact's dimension in the gelatin-phantom demonstrated that in the sagittal

22

case the artifact may consistently spread following the temperature trend until reaching a volume 8 times bigger than the ablated one.

Regarding the artifact distribution dependence on the orientation of the probe with respect to B_0, this is probably because by changing the orientation and shape of the heating pattern the susceptibility distribution can also change, and consequently the artifact shape (Sprinkhuizen *et al.*, 2010). This analysis confirmed that having the laser applicator positioned parallel to B_0 leads to bigger artifact distribution along the sagittal plane (Viallon *et al.*, 2010). More studies should be performed to verify the effect of placing the fiber applicator parallel to B_0. Such configuration could potentially minimize susceptibility artifacts, but it is less used in clinical practice.

On the other hand, concerning the estimation of the temperature error, Viallon et al. (Viallon *et al.*, 2010) used fluoroptic sensors in a few points finding both areas of temperature underestimation and overestimation in correspondence of the positive and negative lobes. In our analysis, the use of FBGs array guarantees the estimation of the absolute temperature error along an entire line of pixels. Therefore, a spatial analysis of the absolute temperature error was performed by distinguishing three main areas of error labeled as *Error_NoArtifacts*, *Error_Artifact*, and *NoError*. Results demonstrate three different trends for the temperature error with the biggest values for the *Error_Artifact* area. The maximum error of 49.7 °C and 64.4 °C, was found for Test1 and Test2, respectively. Comparison with sensing needles allows observing also the absence of a cooling phase in the susceptibility artifact area. Hence, the double-lobe shape does not disappear after switching off the laser and this is probably due to the presence of the bubbles also when irradiation is over.

Additionally, the combined use of three sensing needles allows extracting a 2D thermal map which can potentially integrate and correct the misleading information found in the MRTI. Despite the potential of combining multiple and complementary approaches to measure the correct temperature, more sensors are required to obtain accurate 2D temperature reconstruction with optical fibers thus limiting the minimal invasiveness. Also, the temperature sensing needles should be placed in the area of the artifact for complete and effective integration of information. Then, the limited number of sensing points as well as the different spatial resolution of using multiple sensing needles can be mitigated by means of supporting models, such as data assimilation framework, for the reconstruction of the spatiotemporal profile of the tissue temperature during LITT (Schulmann *et al.*, 2022).

Seeing the temperature error entity and the consequent miscalculation of thermal damage produced, methods to correct susceptibility artifacts should be included in the clinical routine. Several studies proposed simulation-based or T_1-based measurement correction for PRFS thermometry error (Viallon *et al.*, 2010; McLean *et al.*, 2021)·(Baron *et al.*, 2014). Despite the potential of such strategies, they are far from being a standard practice. Also, the unpredictable

distribution of bubbles in tissue complicates a correction based on MR data alone. Additional and highly performant systems to measure temperature can be included in the MRI-guided LA treatment to correct and minimize errors in thermal damage prediction (such as fiber optic sensors). An alternative strategy may consist of real-time control bubble formation to completely avoid any appearance of susceptibility artifacts. Seen the interest for approaches combining thermal and mechanical effects of HIFU to enhance heating and create larger lesions (Sokka, King and Hynynen, 2003), several investigations have already been made to simultaneously monitor both temperature increase and bubbles formation phenomena (Arvanitis and McDannold, 2013).

The following aspects may impact the results of the analysis. The choice of the reference area for the B_0 drift correction may affect the final temperature values measured with the MRTI technique and the resulting susceptibility artifact segmentation. More advanced online drift correction techniques should be used in the future to improve data processing and results (Bing *et al.*, 2016). Also, the MRTI spatial resolution does not correspond exactly to the FBGs dimensions thus a mismatch between the MRTI pixel and FBGs sensor might occur causing possible differences in the extracted absolute temperature error. Further analysis should be performed for the *in vivo* case also including areas of temperature overestimation, perhaps involving additional FBGs properly placed. In such an application, temperature error linked to tissue motion might also affect the efficacy of treatment monitoring.

According to our analysis, artifacts appear when a power of 2 W is set. Previous analysis also showed artifacts formation for a lower value of 1 W and dependence upon the power value (De Landro, Giraudeau, *et al.*, 2022; De Landro, La Pietra, *et al.*, 2022). We decided to show in the manuscript the 2W case as one of the smallest values used in the clinics with bare fiber (Di Matteo *et al.*, 2018). These results demonstrate that the artifact may form under specific heating conditions and probably when a fast temperature increase is induced within a small tissue portion inducing gas-bubble formation or unwanted tissue effects.

Previous works already proposed the combined use of FBGs with MRTI where fiber optic sensors were used as a reference system to evaluate MRTI performances (Allegretti *et al.*, 2015; De Landro *et al.*, 2020, 2021). In this work, FBGs were used to estimate temperature error and to implement the controlled LITT. Our group has already proposed closed-loop strategies finding promising results (Korganbayev *et al.*, 2020, 2021)·(Bianchi *et al.*, 2021) in using FBGs temperature info acquired at a certain distance from the laser source. This is the first time that temperature-controlled LITT based on accurate FBGs values is performed inside an MRI scanner. MRTI commercial systems exploit an open-loop control strategy where specific temperature thresholds are set by the physician which specifies maximum temperature limits for selected critical points. Once the thresholds are overcome, the laser system is switched off. In this case, the controlled temperature values are directly provided by MRTI (McNichols *et al.*, 2004)(Feng and Fuentes, 2011)(Sun *et al.*, 2005). Although the benefits of controlling three-dimensional MRTI maps of the

24

target, including tumoral, healthy tissue, and the area close to the laser applicator tip, this approach may be risky when artifacts affecting the temperature values reliability appear. In our approach, the strategy control is based on multi-point temperature values acquired at 0.3 cm far from the laser source which are indeed very accurate. Furthermore, a PID control strategy is implemented to keep a specific temperature threshold for a set time to finally control the effect of laser-tissue interaction avoiding any unwanted phenomena causing susceptibility artifacts as well as a heat trap. The selected threshold temperature was associated with laser power <1 W (for the used bare applicator) and a specific rate of heating which has allowed to avoid the onset of the artifact. Also, a first linear phase was set which allows the gradually reaching of the chosen threshold. When the laser light-tissue interaction is too intense, the heat may easily produce carbonization because the loss of water causes poor light conduction. On the other hand, a lower level of laser light intensity makes dehydration take place more slowly (Pacella and Mauri, 2020). Such a strategy has been proposed also in *in vivo* LITT (McNichols *et al.*, 2004), the use of a "pre-treatment'' dose appears to anneal the tissue so that subsequent higher power results in more uniform heating without incurrence of unwanted effects. Temperature-controlled LITT enabled the absence of susceptibility artifacts and appreciable thermal damage in the post-ablation MRI images even if tiny. On the other hand, when a small power of 0.5 W is set, even if artifacts may be avoided, no damage can be estimated in the MRI acquired after ablation treatment (see Figure 10b). The maximum temperature values measured after 5 minutes of LITT for 0.5 W and temperature-controlled strategy are ~33 °C and 43 °C, respectively. Therefore, more effective treatment can be achieved in the second case whereas the use of low power may potentially induce consistent coagulation only in a limited portion and by increasing the delivery time. Such an approach could also produce unwanted tissue effects if no control of the temperature is performed. The drawback related to the small ablation dimension can be overcome through a longer treatment time and by using different typologies of the laser applicator, such as diffusive or radial shape applicators embedding cooling methods. Hence, the larger region of light irradiation enables a bigger ablation zone and less focused light intensity thus minimizing carbonization and cavity formation. Besides the promising features, previous experiences suggest otherwise, and undesirable thermal effects may persist (Sean M Munier *et al.*, 2020).

5   Conclusions

MRTI-guided LITT provides effective real-time intraoperative monitoring of the treatment outcome. Nevertheless, there exist still several sources of error which may affect temperature estimation and reliability of such technology. Among them, susceptibility artifacts caused by gas bubble formation and unwanted treatment effects in the tissue (e.g., carbonization, vaporization) strongly affect final temperature maps thus impairing the MRTI usability in clinical conditions. Therefore, the use of MRTI alone holds a high risk of predicting misleading and wrong margins of damage causing a non-effective treatment, potentially leaving tumoral cells behind (persistence). Highly dense optical sensors which provide accurate multipoint measures are promising as an extra tool. They could be used to correct the errors in the MRTI images in the

more risky areas thanks to their performances. Also, in future one single fiber could be used for both sensing and delivering purposes thus minimizing the invasiveness of the approach. Additionally, the use of a diffusive laser applicator, the implementation of control-based strategies avoiding unwanted tissue effects, and the integration of systems to monitor microbubbles activity during the treatment may provide a crucial tool to obtain optimal MRTI-based thermal damage monitoring.

Fundings

Acknowledgments

Ethical statement

The study received full approval from the Institutional Ethical Committee of the Institute of Image-Guided Surgery of Strasbourg (Protocol 38.2015.01.118) and the French Ministry of Superior Education and Research (Project authorization APAFiS#19543-2019030112087889). It was conducted in compliance with French laws for animal use and care and according to the European Directive 2010/63 and with the 3Rs principles (Replacement, Refinement, and Reduction), and developed in congruence with the best welfare animal conditions.

References

Allegretti, G. *et al.* (2015) 'Magnetic resonance-based thermometry during laser ablation on ex-vivo swine pancreas and liver', *Medical Engineering and Physics*. Elsevier Ltd., 37(7), pp. 631–641. doi: 10.1016/j.medengphy.2015.04.001.
Arvanitis, C. D. and McDannold, N. (2013) 'Integrated ultrasound and magnetic resonance imaging for simultaneous temperature and cavitation monitoring during focused ultrasound therapies', *Medical Physics*, 40(11), pp. 1–14. doi: 10.1118/1.4823793.
Baron, P. *et al.* (2014) 'Correction of proton resonance frequency shift MR-thermometry errors caused by heat-induced magnetic susceptibility changes during high intensity focused ultrasound ablations in tissues containing fat', *Magnetic Resonance in Medicine*. John Wiley & Sons, Ltd, 72(6), pp. 1580–1589. doi:

https://doi.org/10.1002/mrm.25063.

Bianchi, L. *et al.* (2021) 'Quasi-distributed fiber optic sensor-based control system for interstitial laser ablation of tissue: theoretical and experimental investigations', *Biomedical Optics Express*, 12(5), p. 2841. doi: 10.1364/boe.419541.

Bianchi, L. *et al.* (2022) 'Thermophysical and mechanical properties of biological tissues as a function of temperature: a systematic literature review', *International Journal of Hyperthermia*. Taylor & Francis, 39(1), pp. 297–340. doi: 10.1080/02656736.2022.2028908.

Bing, C. *et al.* (2016) 'Drift correction for accurate PRF-shift MR thermometry during mild hyperthermia treatments with MR-HIFU', *International Journal of Hyperthermia*. Taylor & Francis, 32(6), pp. 673–687. doi: 10.1080/02656736.2016.1179799.

Chu, K. F. and Dupuy, D. E. (2014) 'Thermal ablation of tumours: biological mechanisms and advances in therapy', *Nature Reviews Cancer*. Nature Publishing Group, 14(3), p. 199.

Di Costanzo, G. G., Francica, G. and Pacella, C. M. (2014) 'Laser ablation for small hepatocellular carcinoma: State of the art and future perspectives', *World Journal of Hepatology*. doi: 10.4254/wjh.v6.i10.704.

Feng, Y. and Fuentes, D. (2011) 'Model-based planning and real-time predictive control for laser-induced thermal therapy.', *International journal of hyperthermia : the official journal of European Society for Hyperthermic Oncology, North American Hyperthermia Group*, 27(8), pp. 751–761. doi: 10.3109/02656736.2011.611962.

Ishihara, Y. *et al.* (1995) 'A precise and fast temperature mapping using water proton chemical shift.', *Magnetic resonance in medicine*. United States, 34(6), pp. 814–823. doi: 10.1002/mrm.1910340606.

Khokhlova, T. D. *et al.* (2009) 'Magnetic resonance imaging of boiling induced by high intensity focused ultrasound', *The Journal of the Acoustical Society of America*, 125(4), pp. 2420–2431. doi: 10.1121/1.3081393.

Korganbayev, S. *et al.* (2020) 'Closed-Loop Temperature Control Based on Fiber Bragg Grating Sensors for Laser Ablation of Hepatic Tissue', *Sensors*. doi: 10.3390/s20226496.

Korganbayev, S. *et al.* (2021) 'PID Controlling Approach Based on FBG Array Measurements for Laser Ablation of Pancreatic Tissues', *IEEE Transactions on Instrumentation and Measurement*. IEEE, 70, p. 1. doi: 10.1109/TIM.2021.3112790.

Laimer, G. *et al.* (2020) 'Minimal ablative margin (MAM) assessment with image fusion: an independent predictor for local tumor progression in hepatocellular carcinoma after stereotactic radiofrequency ablation.', *European radiology*, 30(5), pp. 2463–2472. doi: 10.1007/s00330-019-06609-7.

De Landro, M. *et al.* (2020) 'Fiber Bragg Grating Sensors for Performance Evaluation of Fast Magnetic Resonance Thermometry on Synthetic Phantom', *Sensors* . doi: 10.3390/s20226468.

De Landro, M. *et al.* (2021) 'Magnetic resonance-based measurement system: comparison of 2D and 3D echo-planar imaging sequences for thermometry application', in *2021 IEEE International Instrumentation and Measurement Technology Conference (I2MTC)*, pp. 1–6. doi: 10.1109/I2MTC50364.2021.9460088.

De Landro, M., La Pietra, F., *et al.* (2022) 'Analysis of cavitation artifacts in Magnetic Resonance Imaging Thermometry during laser ablation monitoring', in *2022 44th Annual International Conference of the IEEE Engineering in Medicine & Biology Society (EMBC)*, pp. 5008–5011. doi: 10.1109/EMBC48229.2022.9871675.

De Landro, M., Giraudeau, C., *et al.* (2022) 'Characterization of Susceptibility Artifacts in MR-thermometry PRFS-based during Laser Interstitial Thermal Therapy', in *2022 IEEE International Symposium on Medical Measurements and Applications (MeMeA)*, pp. 1–5. doi: 10.1109/MeMeA54994.2022.9856421.

Makowka, L. *et al.* (1988) 'Surgical technique of orthotopic liver transplantation.', *Gastroenterology clinics of North America*, 17(1), pp. 33–51.

Di Matteo, F. M. *et al.* (2018) 'Feasibility of EUS-guided Nd:YAG laser ablation of unresectable pancreatic adenocarcinoma', *Gastrointestinal Endoscopy*. doi: 10.1016/j.gie.2018.02.007.

McLean, M. *et al.* (2021) 'A T1-based correction method for proton resonance frequency shift thermometry in breast tissue.', *Medical physics*, 48(9), pp. 4719–4729. doi: 10.1002/mp.15085.

27

McNichols, R. J. *et al.* (2004) 'MR Thermometry-Based Feedback Control of Laser Interstitial Thermal Therapy at 980 nm', *Lasers in Surgery and Medicine*, 34(1), pp. 48–55. doi: 10.1002/lsm.10243.

Morra, F. *et al.* (2020) 'Spatially resolved thermometry during laser ablation in tissues: Distributed and quasi-distributed fiber optic-based sensing', *Optical Fiber Technology*. Elsevier, 58, p. 102295.

Munier, Sean M., Liang, A. S., *et al.* (2020) 'Characterization of magnetic resonance thermal imaging signal artifact during magnetic resonance guided laser-induced thermal therapy', *Operative Neurosurgery*, 19(5), pp. 619–624. doi: 10.1093/ons/opaa229.

Munier, Sean M *et al.* (2020) 'Effects of Intraoperative Magnetic Resonance Thermal Imaging Signal Artifact During Laser Interstitial Thermal Therapy on Thermal Damage Estimate and Postoperative Magnetic Resonance Imaging Ablative Area Concordance.', *Operative neurosurgery (Hagerstown, Md.)*. United States, 18(5), pp. 524–530. doi: 10.1093/ons/opz182.

Munier, Sean M., Desai, A. N., *et al.* (2020) 'Effects of intraoperative magnetic resonance thermal imaging signal artifact during laser interstitial thermal therapy on thermal damage estimate and postoperative magnetic resonance imaging ablative area concordance', *Operative Neurosurgery*, 18(5), pp. 524–530. doi: 10.1093/ons/opz182.

Nikfarjam, M., Muralidharan, V. and Christophi, C. (2005) 'Mechanisms of focal heat destruction of liver tumors', *Journal of Surgical Research*, 127(2), pp. 208–223. doi: 10.1016/j.jss.2005.02.009.

Odéen, H. and Parker, Dennis L. (2019a) 'Improved MR thermometry for laser interstitial thermotherapy', *Lasers in Surgery and Medicine*. doi: 10.1002/lsm.23049.

Odéen, H. and Parker, Dennis L. (2019b) 'Improved MR thermometry for laser interstitial thermotherapy', *Lasers in Surgery and Medicine*. doi: 10.1002/lsm.23049.

Odéen, H. and Parker, Dennis L. (2019c) 'Magnetic resonance thermometry and its biological applications – Physical principles and practical considerations', *Progress in Nuclear Magnetic Resonance Spectroscopy*, 110, pp. 34–61. doi: 10.1016/j.pnmrs.2019.01.003.

Odéen, H. and Parker, Dennis L (2019) 'Magnetic resonance thermometry and its biological applications – Physical principles and practical considerations', *Progress in Nuclear Magnetic Resonance Spectroscopy*, 110, pp. 34–61. doi: https://doi.org/10.1016/j.pnmrs.2019.01.003.

Pacella, C. M. and Mauri, G. (2020) *Image-guided laser ablation*. Springer.

Parker, D. L., Payne, A. and Odéen, H. (2022) 'A k-space-based method to measure and correct for temporal B0 field variations in MR temperature imaging', *Magnetic Resonance in Medicine*. John Wiley & Sons, Ltd, 88(3), pp. 1098–1111. doi: https://doi.org/10.1002/mrm.29275.

Patel, P., Patel, N. V. and Danish, S. F. (2018) 'Laser interstitial thermal therapy', *Functional Neurosurgery and Neuromodulation*, pp. 153–176. doi: 10.1016/B978-0-323-48569-2.00021-5.

De Poorter, J. (1995) 'Noninvasive MRI thermometry with the proton resonance frequency method: study of susceptibility effects.', *Magnetic resonance in medicine*. United States, 34(3), pp. 359–367. doi: 10.1002/mrm.1910340313.

Salem, U. *et al.* (2019) 'Neurosurgical applications of MRI guided laser interstitial thermal therapy (LITT)', *Cancer Imaging*, 19(1), p. 65. doi: 10.1186/s40644-019-0250-4.

Schulmann, N. *et al.* (2022) 'Model-Based Thermometry for Laser Ablation Procedure Using Kalman Filters and Sparse Temperature Measurements', *IEEE Transactions on Biomedical Engineering*. IEEE.

Senneville, B. D. *et al.* (2007) 'MR thermometry for monitoring tumor ablation', *European Radiology*, 17(9), pp. 2401–2410. doi: 10.1007/s00330-007-0646-6.

Sokka, S. D., King, R. and Hynynen, K. (2003) 'MRI-guided gas bubble enhanced ultrasound heating in in vivo rabbit thigh.', *Physics in medicine and biology*. England, 48(2), pp. 223–241. doi: 10.1088/0031-9155/48/2/306.

Sprinkhuizen, S. M. *et al.* (2010) 'Temperature-induced tissue susceptibility changes lead to significant temperature errors in PRFS-based MR thermometry during thermal interventions.', *Magnetic resonance in medicine*. United States, 64(5), pp. 1360–1372. doi: 10.1002/mrm.22531.

Stafford, R. J. *et al.* (2010) 'Laser-induced thermal therapy for tumor ablation', *Critical Reviews in Biomedical Engineering*. Begel House Inc., 38(1), pp. 79–100. doi: 10.1615/CritRevBiomedEng.v38.i1.70.

Sun, L. *et al.* (2005) 'Adaptive real-time closed-loop temperature control for ultrasound hyperthermia using magnetic resonance thermometry', *Concepts in Magnetic Resonance Part B: Magnetic Resonance Engineering*, 27B(1), pp. 51–63. doi: 10.1002/cmr.b.20046.

Viallon, M. *et al.* (2010) 'Observation and correction of transient cavitation-induced PRFS thermometry artifacts during radiofrequency ablation, using simultaneous Ultrasound/MR imaging', *Medical Physics*, 37(4), pp. 1491–1506. doi: 10.1118/1.3309439.

Walser, E. *et al.* (2019) 'Focal Laser Ablation of Prostate Cancer: Results in 120 Patients with Low- to Intermediate-Risk Disease', *Journal of Vascular and Interventional Radiology*. Elsevier, Inc, 30(3), pp. 401-409.e2. doi: 10.1016/j.jvir.2018.09.016.

Winter, L. *et al.* (2016) 'Magnetic resonance thermometry: Methodology, pitfalls and practical solutions', *International Journal of Hyperthermia*. doi: 10.3109/02656736.2015.1108462.